Achieving a Large Energy Gap in Bi(110) Atomically Thin Films

Qing Yuan, Yafei Li, Deping Guo, Cancan Lou, Xingxia Cui, Guangqiang Mei, Chengxiang Jiao, Kai Huang, Xuefeng Hou, Wei Ji, Limin Cao,* and Min Feng**

Metal–insulator transition has long been one of the key subjects in condensed matter systems. Herein, the emergence of a large energy gap (E_g, 0.8–1.0 eV) in Bi(110) two-atomic-layer nanoribbons grown on a SnSe(001) substrate is reported, which normally has an intrinsic semimetal-like characteristic. The existence of this abnormally large E_g in Bi(110) is, however, determined by Bi coverage. When coverage is above ≈64 ± 2%, E_g vanishes, and instead, a Bi(110) semimetal-like phase appears through a singular insulator–metal transition. Measurements using qPlus atomic force microscopy demonstrate that either insulating or semimetal-like Bi(110) possesses a distorted black phosphorous structure with noticeable atomic buckling. Density function theory fully reproduces the semimetal-like Bi(110) on SnSe(001). However, none of the insulating phases with this large E_g could be traced. Although the underlying mechanism of the large E_g and the insulator-metal transition requires further exploration, experiments demonstrate that similar results can be achieved for Bi grown on SnS, the structural analog of SnSe, exhibiting an even larger E_g of ≈2.3 eV. The experimental strategy may be generalized to utilization of group-IV monochalcogenides to create Bi(110) nanostructures with properties unachievable on other surfaces, providing an intriguing platform for exploring the interesting quantum electronic phases.

1. Introduction

Engineering interfacial coupling between ultrathin films and substrates facilitates opportunities to create new materials with electronic properties completely different from those of their bulk counterparts.[1–5] Being a heavy element with unique and anomalous electronic properties, the semimetal bismuth (Bi) is one of the most extensively studied materials and has played an exceptional role in revealing many interesting phenomena in solid-state physics.[6–12] In particular, ultrathin Bi films have provided a representative platform for fundamental and technological explorations through delicate tailoring of their atomic and electronic structures,[13–21] interfacial structure,[2,3,22–25] charge doping,[21,26] etc. When Bi is deposited on alternative substrates with a few-layer atomic thickness, such as Si(111),[27] highly oriented pyrolytic graphite (HOPG),[13,22,28] epitaxial graphene,[23,29] $NbSe_2$,[21,26] and ferromagnetic Fe_3GeTe_2,[25] Bi normally forms Bi(110)-oriented thin films. Bi(110) atomic films show a biatomic layer stacking structure similar to that of black phosphorus (BP), where each unit cell of the Bi(110) atomic layer contains two Bi atoms. According to the atomic buckling height, Δh, of the two Bi atoms, the Bi(110) films are categorized as BP structures with flat surfaces ($\Delta h = 0$) and distorted BP (DBP) structures ($\Delta h \neq 0$). Few-layer Bi(110) thin films have attracted extensive attention due to their discovery of a series of exotic quantum phenomena. For example, BP-like Bi(110) on graphene has been reported to be an elemental 2D topological insulator (TI) with well-localized topological edge states,[13,28] while its bulk energy gap is less than 100 meV.

Atomic buckling has been predicted to be important for modulating the electronic properties of ultrathin Bi(110) layers.[13–16] Despite extensive studies on Bi(110) films grown on various

Q. Yuan, Y. Li, C. Lou, X. Cui, G. Mei, C. Jiao, K. Huang, X. Hou, L. Cao, M. Feng
School of Physics and Technology and Key Laboratory of Artificial Micro- and Nano-Structures of Ministry of Education
Wuhan University
Wuhan 430072, China
E-mail: limincao@whu.edu.cn; fengmin@whu.edu.cn

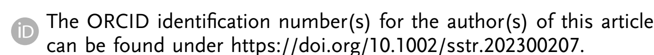
The ORCID identification number(s) for the author(s) of this article can be found under https://doi.org/10.1002/sstr.202300207.

© 2023 The Authors. Small Structures published by Wiley-VCH GmbH. This is an open access article under the terms of the Creative Commons Attribution License, which permits use, distribution and reproduction in any medium, provided the original work is properly cited.

DOI: 10.1002/sstr.202300207

D. Guo, W. Ji
Beijing Key Laboratory of Optoelectronic Functional Materials & Micro-Nano Devices
Department of Physics
Renmin University of China
Beijing 100872, China
E-mail: wji@ruc.edu.cn

D. Guo, W. Ji
Key Laboratory of Quantum State Construction and Manipulation (Ministry of Education)
Renmin University of China
Beijing 100872, China

M. Feng
Institute for Advanced Study
Wuhan University
Wuhan 430072, China

substrates,[13,21,23,25–29] experimental proof of the creation of DBP Bi(110) with atomically resolved Δh and exploration of its associated electronic structures have been limited. In our study, we introduced substrates with a DBP structure,[30–35] such as SnSe(001), aiming to induce atomic buckling in Bi(110) to modulate its electronic properties. Through van der Waals (vdW) epitaxy, two-atomic-layer (2-AL) Bi(110) nanoribbon thin films with different Bi coverages were grown on SnSe(001) surfaces. Utilizing qPlus noncontact atomic force microscopy (qPlus nc-AFM), we directly characterized and confirmed nonuniform atomic buckling structures in the formed Bi(110) atomic thin films, which had a measured maximum Δh of less than 6.2 ± 1.5 pm. However, scanning tunneling microscopy/spectroscopy (STM/STS) showed that the electronic structures of the grown Bi(110) were categorized into two distinct phases depending on the coverage of Bi. When the coverage was less than $\approx 64 \pm 2\%$, an anomalous large energy gap (E_g) of 0.8–1.0 eV emerged in Bi(110) nanoribbon thin films. However, when the coverage of Bi on SnSe was more than $\approx 64 \pm 2\%$, it underwent an abrupt insulator–metal transition into the semimetal-like state. The semimetal-like phases of Bi(110) with DBP structures were predicted in previous studies[21,25,26] and were verified by our density function theory (DFT) calculations. However, this insulating phase with its large E_g of 0.8–1.0 eV was beyond the scope of current theoretical work based on its induction via atomic buckling.

Furthermore, our qPlus AFM measurements showed that upon the formation of insulating Bi(110) nanoribbons, the Sn–Se atomic zigzag (ZZ) chains adjacent to insulating Bi nanoribbons were unexpectedly pulled up to 20.4 ± 1.5 pm, higher than those farther away from Bi. This distortion was accompanied by an ≈ 0.5 eV downshift of the valence band maximum (VBM) with a negligible change in the conduction band minimum (CBM) in SnSe close to Bi; this result could be effectively reproduced by our DFT calculations. Therefore, our work supports the fact that there is strong interfacial coupling between Bi(110) and SnSe(001), which leads to pulling-up of the SnSe(001) atomic layer(s) underneath Bi and introduces a consecutive distortion of the adjacent SnSe atomic chains. Our experiments further showed that the phenomena observed for Bi on SnSe could be generalized for Bi on group-IV monochalcogenides MX (M = Sn or Ge and X = S or Se) with DBP structures. On the SnS substrate, the Bi(110) 2-AL thick nanoribbons have an even larger E_g of ≈ 2.3 eV and experience an insulator–metal-like phase transition when the coverage of Bi(110) nanoribbons is more than $\approx 80 \pm 2\%$ on SnS substrates.

2. Results and Discussion

The 2-AL Bi(110) nanoribbon thin films were grown on SnSe(001) and SnS(001) substrates through vdW epitaxy at room temperature (RT). **Figure 1**a shows the side- and top-view atomic models of a 2-AL Bi(110) layer residing on SnSe(001) substrate. As schematically shown in the model, the BP-structured 2-AL Bi(110) has Bi atoms propagating in chains along the zigzag (ZZ) direction and troughs in the orthogonal armchair (AC) direction. In each AL, a unit cell of Bi (denoted by the black rectangle in Figure 1a) contains two Bi atoms (denoted Bi_A–Bi_B), forming a Bi–Bi dimer, which is unpuckered on isotropic substrates such as HOPG.[13,28] The SnSe(001) substrate has a DBP structure in which Sn atoms are slightly elevated above the neighboring Se atoms.[30–35] Figure 1b shows a typical STM image of an as-grown Bi nanoribbon thin film with a coverage of $\approx 46 \pm 2\%$ on the SnSe surface. Under positive biases, Bi nanoribbons exhibit a waffle-like rectangular superstructure composed of rectangular supercells, as marked by the blue-dashed rectangle in the inset in Figure 1b. Bi nanoribbons elongate along the zigzag direction of SnSe, as verified by the atom-resolved Sn–Se ZZ chains shown by qPlus AFM imaging (Figure 1c). The height line profiles of Sn and Se atoms along the AC direction (as labeled by the red and black arrows in Figure 1c) show a measured atomic height difference of 24.7 ± 1.5 pm, consistent with the theoretically predicted value of ≈ 29.0 pm (Figure S1, Supporting Information). Considering that the qPlus AFM results could slightly vary depending on the scanning parameter used, Δf, we performed control experiments under different conditions to measure the atomic heights of Sn and Se atoms. Our results show that the measured values only slightly vary when Δf is in a certain range (Figure S2, Supporting Information). This confirms that the AFM results can reproducibly reflect the spatial atomic height difference at the surface when Δf is carefully chosen.

The nanoribbon thin film has a typical AFM measured height of 698.5 ± 1.5 pm (Figure 1d), consistent with our theoretical value and the experimental values reported for 2-AL BP-like Bi(110) on HOPG.[13,22,28] An atom-resolved STM image (Figure 1e) shows the atomic configuration of the rectangular supercell (marked by the blue-dashed rectangle in Figure 1e) with clearly resolved Bi_A and Bi_B atoms in the Bi(110) ZZ chains. Combined with the atom-resolved AFM imaging in Figure 1f, we determine that the rectangular Bi(110) supercell is composed of 11×11 Bi ZZ chains and AC rows. Based on the observed alignment of the Bi and SnSe ZZ chains and the measured lattice constants of Bi and SnSe (4.8 ± 0.2 (AC) and 4.5 ± 0.2 (ZZ) Å for Bi; 4.4 ± 0.2 (AC) and 4.1 ± 0.2 (ZZ) Å for SnSe), we identify that Bi forms a Bi(110)-11×11/SnSe(001)-12×12 Moiré superlattice. Although the Bi_A and Bi_B atoms in the Bi(110) unit cell are of similar STM contrast in Figure 1e, they are considerably different in AFM imaging (Figure 1f). As illustrated by the height line profiles (Figure 1g) of Bi_A and Bi_B atoms along the AC direction (marked by black- and red-dashed arrows in Figure 1f), pronounced buckling of Bi_A–Bi_B atomic pairs occurs in one atomic unit cell. Furthermore, the atomic buckling is nonuniform within one supercell, showing a typical maximum Δh of 3.8 ± 1.5 pm. We carried out AFM measurements with different tips and scanning parameters (Figure S3, Supporting Information), and they provided similar Δh values. This enabled verification of the result that the magnitude of Δh is less than 10.0 pm. Since the AFM image contrast dominantly records the atomic height variation, our results clearly confirm that the 2-AL Bi(110) grown on the SnSe(001) surface has the DBP structure.

In addition to experimentally confirming the atomic buckling structure in the Bi nanoribbon, we further performed detailed STS measurements to study its electronic properties. **Figure 2**a shows a series of STS dI/dV spectra acquired from four typical locations in the Bi(110) supercell. A common feature of the

© 2023 The Authors. Small Structures published by Wiley-VCH GmbH

26884062, 2023, 12, Downloaded from https://onlinelibrary.wiley.com/doi/10.1002/sstr.202300207 by RENMIN UNIVERSITY OF CHINA NON-EAL ACCOUNT, Wiley Online Library on [23/04/2024]. See the Terms and Conditions (https://onlinelibrary.wiley.com/terms-and-conditions) on Wiley Online Library for rules of use; OA articles are governed by the applicable Creative Commons License

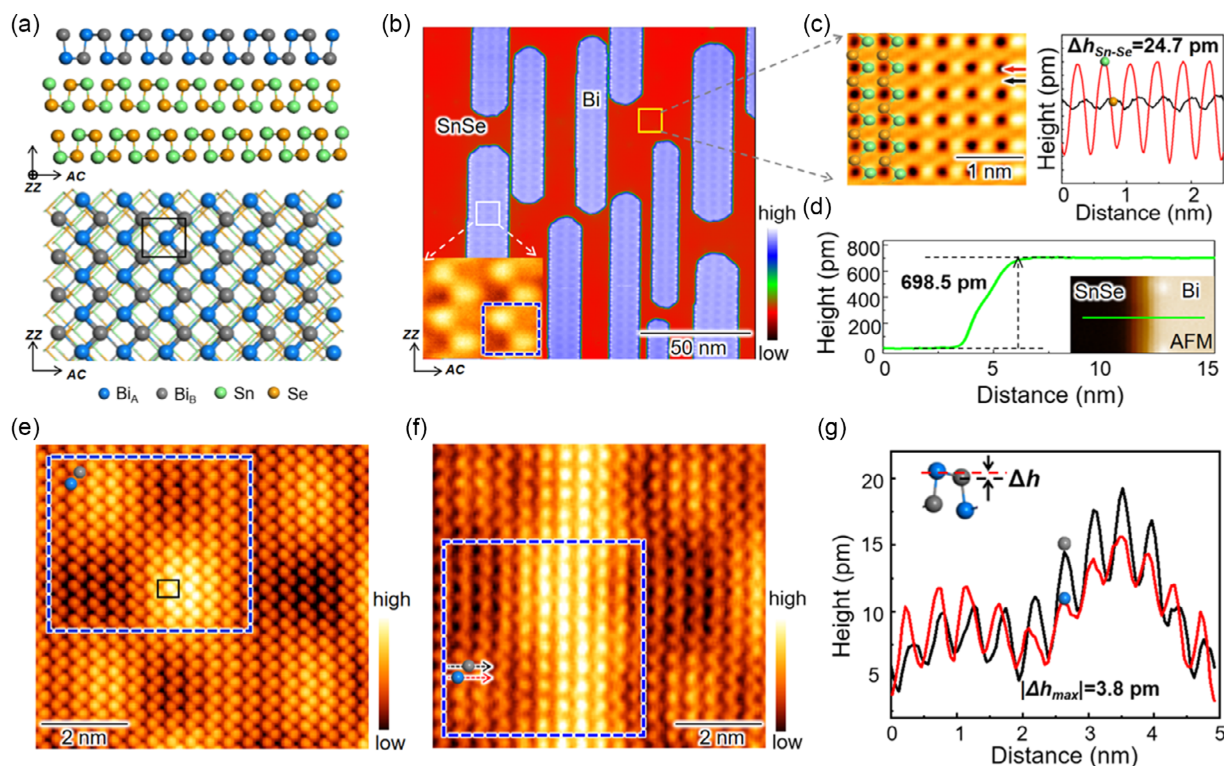

Figure 1. Atomic structures of 2-AL Bi(110) on the SnSe(001) substrate. a) Schematic side- and top-views of 2-AL Bi(110) on the SnSe(001) surface. The black rectangle marks the atomic unit cell of Bi(110) containing Bi_A and Bi_B atoms. b) STM image ($V = 1.8$ V, $I = 5$ pA) of Bi(110) nanoribbons on SnSe(001). The nanoribbons preferentially grow with the elongation direction along the ZZ direction of the SnSe substrate. The inset shows the typical STM contrast of the Bi(110) supercell acquired at $V = 0.87$ V and $I = 5$ pA, where the blue-dashed rectangle marks a supercell. c) Atom-resolved AFM image ($\Delta f = -1.18$ Hz) of the SnSe substrate marked by the yellow square in (b). The atomic model is superposed on the AFM image to locate Sn and Se atoms. AFM line profiles along Sn and Se atomic rows marked by the black and red arrows in (c) along the AC direction are shown in the right panel. d) AFM height profile of the Bi nanoribbon measured along the AC direction (shown in the inset). e) Atom-resolved STM image ($V = 0.87$ V, $I = 1.28$ nA) of the Bi(110) nanoribbon, with the blue-dashed rectangle marking the supercell and the black rectangle marking the atomic unit cell. f) Atom-resolved AFM image ($\Delta f = -9.90$ Hz) of Bi(110). The blue-dashed rectangle marks the supercell. g) AFM line profiles examined along Bi_A and Bi_B atomic rows (marked by the black and red arrows in (f) along the AC direction. The atomic buckling height Δh between Bi_A and Bi_B in one atomic unit cell is highlighted by the atomic model. CO and/or metallic tungsten tips were used in the measurements.

dI/dV spectra is that each has a pronounced energy gap of ≈0.9 eV (Figure 2b), corresponding to the nearly zero current in the I–V curves (Figure S4, Supporting Information). Bi(110) ultrathin films grown on various alternative substrates normally have semimetal-like characteristics or act as TIs with a very small bulk E_g, originating from the pristine semimetal nature of bulk Bi;[13,21,23,25,26,28,29] our experiments produced drastically different results, with a large E_g emerging in Bi(110) on SnSe. To verify our abnormal E_g, we performed extensive location-dependent STS studies. All STS spectra show the presence of ≈0.9 eV E_g in different regions within the superlattice despite inhomogeneous atomic buckling (Figure S5, Supporting Information). Height-dependent STS spectra show that the bandgap is independent of the electric field applied between the STM tip and the sample (Figure S6, Supporting Information), excluding the possible Stark shift effect on the spectra.[36–39] These results establish the existence of a robust E_g hosted in the Bi(110) superlattice nanoribbons.

To further characterize the grown 2-AL Bi(110) on SnSe(001), we examined the evolution of dI/dV spectra from the middle to edge of the nanoribbon. As shown in Figure 2c, edge states appear when approaching the island edge (Figure S7, Supporting Information). The edge states could be induced by atomic reconstruction at the edge.[13,29] The appearance of edge states causes the energy gap of Bi(110) to shrink to ≈0.7 eV around the edge. This result is another distinct feature of our grown Bi(110) nanostructures compared to those reported. For example, BP-structured Bi(110) on HOPG was verified as a TI, where the dI/dV spectra showed an ≈100 meV gap within the Bi nanoribbon and a gapless edge state at the edge.[13] Bi(110) nanoribbons grown on epitaxial graphene were reported to have a large energy gap of ≈0.4 eV at the center, but the edge was metallic.[29] In our experiments, pronounced E_g is robustly shown over the nanoribbon, both from the body and the edge. Moreover, we acquired a series of STS spectra from Bi nanoribbons with different widths from 9.0 to 45.0 nm. The obtained E_g values are similar, mostly in the range of 0.8–1.0 eV (Figure 2d). Thus, the quantum confinement effect is not considered to be the origin of the energy gap in 2-AL Bi(110) on SnSe. We noticed that in previous work on Bi(110) nanostructures, quantum confinement was not involved either.[13,21,23,25,26,28,29]

© 2023 The Authors. Small Structures published by Wiley-VCH GmbH

26884062, 2023, 12, Downloaded from https://onlinelibrary.wiley.com/doi/10.1002/sstr.202300207 by RENMIN UNIVERSITY OF CHINA NON-EAL ACCOUNT, Wiley Online Library on [23/04/2024]. See the Terms and Conditions (https://onlinelibrary.wiley.com/terms-and-conditions) on Wiley Online Library for rules of use; OA articles are governed by the applicable Creative Commons License

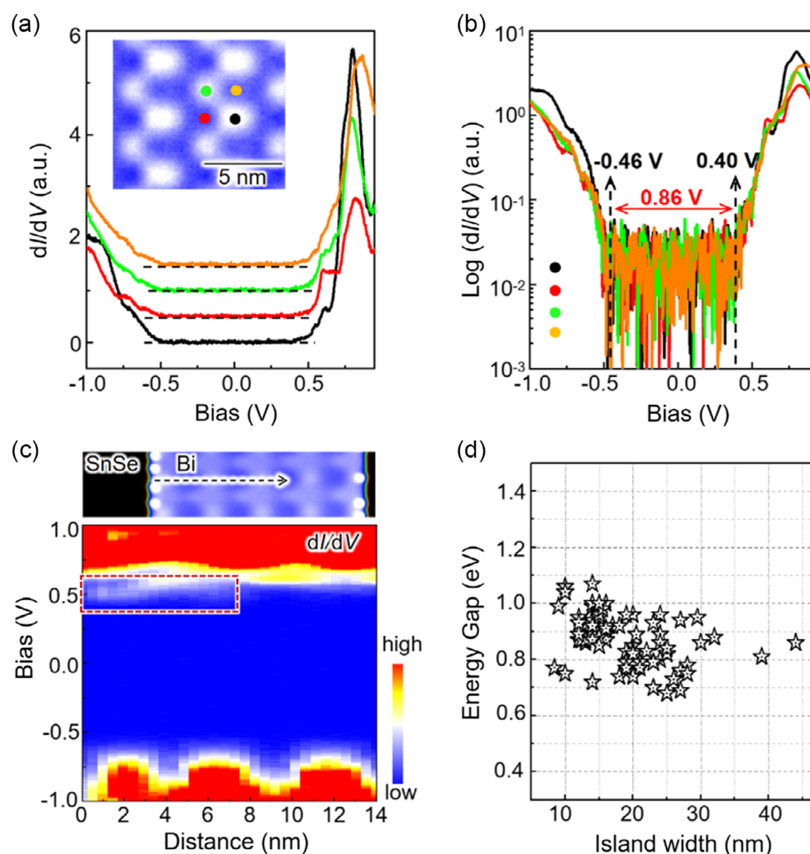

Figure 2. Electronic structures of the 2-AL Bi(110) nanoribbon on the SnSe(001) substrate. a) Typical STS dI/dV spectra acquired at the four typical STM contrast regions in a Bi(110) supercell, marked by the black, red, green, and brown dots in the inset STM image. The spectra lines are offset for clarity. The horizontal black-dashed lines indicate zero conductance in each of the spectra. b) Logarithmic coordinate y-axis for the dI/dV spectra in (a). The energy gap can be visualized more clearly. c) Intensity contour of STS dI/dV spectra acquired from the edge to the interior of the Bi nanoribbon along the AC direction, as marked by the black-dashed arrow in the upper panel STM image. The red-dashed rectangle shows the edge states around the edge. An oscillation seems to appear between −0.5 and −1.0 V in (c). A close examination of the dI/dV spectra, as shown in Figure S8, Supporting Information, reveals that this is caused by deeper energy states rather than the valence edge. This does not influence the valence edge and thus E_g (Figure S8, Supporting Information). d) Measured E_g values from a series of Bi(110) nanoribbons with different widths.

The emergence of the large E_g in Bi(110) on SnSe is anomalous in comparison with previous studies on various Bi(110) thin films grown on different substrates,[13,21,23,25,26,28,29] which were normally an intrinsic semimetal or an atomic buckling-induced TI. It was predicted that 2-AL Bi(110) could also behave as a trivial semiconductor with a very narrow bandgap, which depended on the magnitude of the atomic buckling (Δh).[13,16] When Δh is in the range of 0.0–10.0 pm, 2-AL Bi(110) is a nontrivial TI with a bulk gap of less than ≈100 meV; however, when $\Delta h > 10.0$ pm, it transforms into a trivial narrow-bandgap semiconductor. According to the prediction and considering the largest atomic buckling value (3.8 ± 1.5 pm) experimentally observed in the Bi nanoribbons, the grown Bi(110) should be a TI with E_g less than 50 meV. Additionally, based on the prediction, if the atomic buckling Δh is 50.0 pm, then Bi(110) could produce a bandgap as large as 0.4 eV. However, this is ten times larger than our observed Bi_A–Bi_B atomic buckling value. This case would not occur since the calculated (Figure S1, Supporting Information) and measured (Figure 1c) atomic buckling values between Sn and Se of the SnSe substrate are only ≈29.0 and ≈24.7 pm, respectively. Consequently, 50.0 pm atomic buckling is unlikely to occur in reality for Bi grown on SnSe. Specifically, the presence of atomic buckling alone could not explain the origin of the observed large E_g in 2-AL Bi(110) on SnSe. Bi evaporated on GaAs(110) was reported to have a 0.7 eV energy gap. However, in that case, the Bi atoms hybridized with Ga and As atoms, and an atomic interlayer was formed with a thickness of 260 pm.[24] This was structurally different from the 2-AL Bi(110) with a thickness of 698.5 ± 1.5 pm (Figure 1d).

Since substrates were less frequently investigated in experimental studies of submonolayer films and to further explore this emergent abnormal E_g, we examined the SnSe substrate, especially the regions adjacent to Bi(110) nanoribbons, using qPlus AFM and STM/STS. Our measurements clearly demonstrate that the growth of Bi(110) thin films greatly modifies the atomic and electronic structures of the SnSe surface layer. **Figure 3**a shows an STM topographic image, exhibiting the lateral interface between a Bi(110) nanoribbon and the SnSe(001) substrate. The atom-resolved AFM image of the SnSe region adjacent to the edge of the Bi nanoribbon (marked by the blue rectangle

© 2023 The Authors. Small Structures published by Wiley-VCH GmbH

26884062, 2023, 12, Downloaded from https://onlinelibrary.wiley.com/doi/10.1002/sstr.202300207 by RENMIN UNIVERSITY OF CHINA NON-EAL ACCOUNT, Wiley Online Library on [23/04/2024]. See the Terms and Conditions (https://onlinelibrary.wiley.com/terms-and-conditions) on Wiley Online Library for rules of use; OA articles are governed by the applicable Creative Commons License

26884062, 2023, 12, Downloaded from https://onlinelibrary.wiley.com/doi/10.1002/sstr.202300207 by RENMIN UNIVERSITY OF CHINA NON-EAL ACCOUNT, Wiley Online Library on [23/04/2024]. See the Terms and Conditions (https://onlinelibrary.wiley.com/terms-and-conditions) on Wiley Online Library for rules of use; OA articles are governed by the applicable Creative Commons License

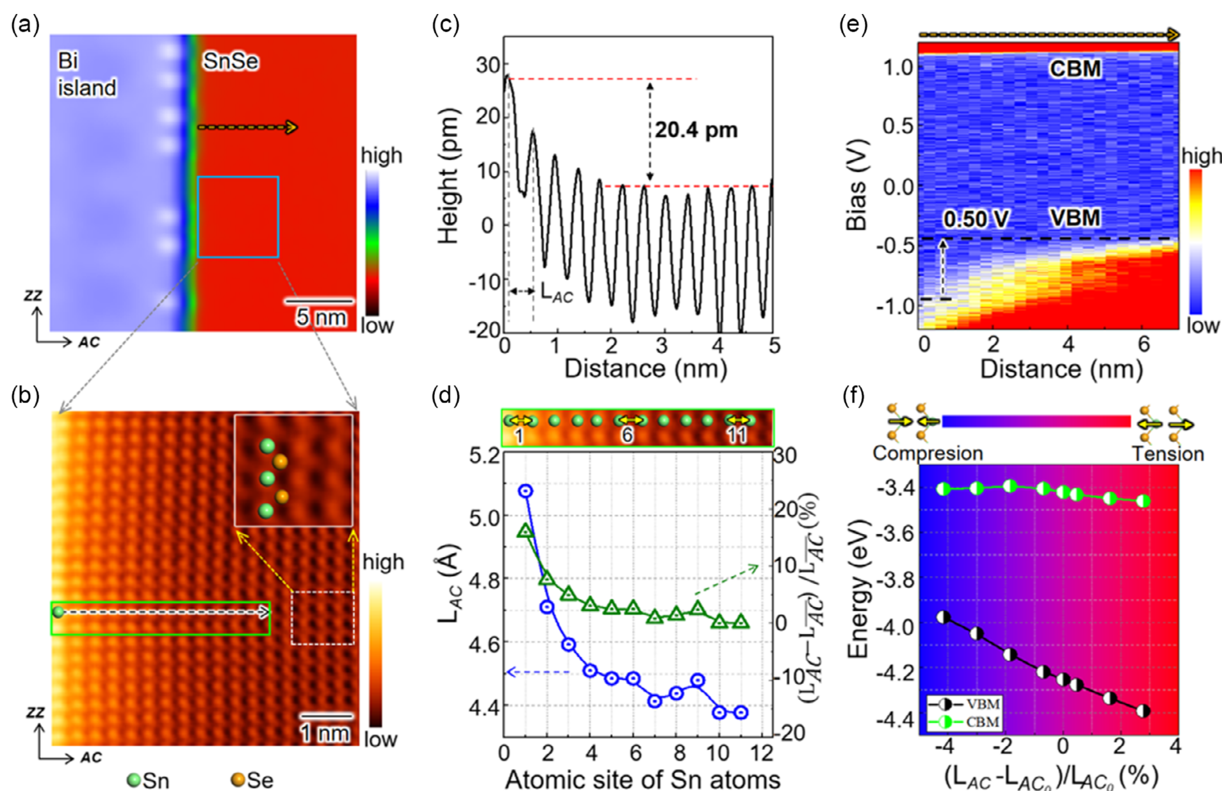

Figure 3. Atomic distortions of the SnSe substrate upon the growth of Bi nanoribbons. a) STM topographic image of a Bi nanoribbon and a SnSe substrate. The blue square marks a typical SnSe region adjacent to the Bi nanoribbon. b) Atom-resolved AFM image ($\Delta f = -14.8$ Hz) of the blue square marked region in (a). The inset shows the amplified image of the white-dashed rectangle marked region, highlighting the resolved Sn and Se atoms. c) AFM line profile of Sn atoms from the interface to the interior of SnSe along the AC direction, which is marked by the black-dashed arrow in (b). L_{AC} denotes the Sn–Sn atomic distance in the AC direction. d) Variation in L_{AC} and corresponding in-plane tensile strain between Sn atoms of SnSe from the Bi–SnSe interface to far from the interface along the AC direction. The green rectangle in the top panel marks the measured region as indicated in (b). $\overline{L_{AC}}$ represents the average Sn–Sn atomic distance measured for regions ≈20 nm away from the Bi nanoribbon on the SnSe surface layer. This distance is almost identical to that of the pure SnSe substrate. e) STS spectrum map acquired along a line from the Bi–SnSe interface away from the Bi nanoribbon in the AC direction (denoted by the orange-dashed arrow in (a). f) DFT-calculated energy positions of the VBM and CBM of 2-AL SnSe under different amounts of compression and/or extension along the AC direction. The energy values of the VBM and CBM are relative to the vacuum energy level. The black (green) dot represents the VBM (CBM). L_{AC0} represents the Sn–Sn atomic distance of pure SnSe in the AC direction.

in Figure 3a) is shown in Figure 3b. The pronounced feature shows that the SnSe ZZ chains close to the Bi nanoribbon present brighter contrast, indicating that they are evidently higher than those chains farther away from Bi. This result is further illustrated in Figure 3c, in which the typical height line profile of Sn atoms in the same AC row is shown. Sn atoms are highest around the island edge, while the height gradually decreases away from the edge and reaches a uniform height after ≈7–8 atomic ZZ chains. A maximum 20.4 ± 1.5 pm height difference is observed between the Sn atoms next to and far from the Bi nanoribbon. In contrast, there is negligible height variation between Sn atoms along the ZZ direction, as shown in Figure S9, Supporting Information. We performed control experiments (Figure S10, Supporting Information) to exclude any tip-induced artifacts in the AFM measurements and verify our observations.

The AFM results indicate that SnSe ZZ atomic chains underneath and next to the Bi nanoribbon are pulled up upon Bi adsorption, which is consequently shown by brighter contrasts and higher profiles of the SnSe ZZ chains around the Bi nanoribbon edge in AFM measurements. Upon pulling-up, the lateral (in the AC direction) lattice constant of SnSe is increased to $\approx 5.1 \pm 0.2$ Å at the location close to the Bi nanoribbon, as shown in Figure 3d. It gradually recovers to the normal Sn–Sn lattice constant on undistorted SnSe(001) surfaces ($\approx 4.4 \pm 0.2$ Å) after a lateral distance of ≈40.0 Å. This corresponds to a lateral tensile strain in the AC direction as high as 16% for the Sn–Sn lattice (green triangles and curve in Figure 3d). In contrast, we discovered that the Sn–Sn atomic distances remain uniform in the ZZ direction regardless of where they are measured (Figure S9, Supporting Information).

The atomic distortions of SnSe ZZ chains are accompanied by a notable influence on the electronic characteristics. Figure 3e shows the intensity contour of the STS dI/dV spectra measured from the Bi–SnSe interface to away from the Bi nanoribbon in the AC direction on SnSe (denoted by the orange-dashed arrow in Figure 3a). Two typical dI/dV spectra in Figure S11, Supporting Information, show the electronic characteristics of SnSe close to and far from the Bi nanoribbon. The VBM of

 © 2023 The Authors. Small Structures published by Wiley-VCH GmbH

SnSe adjacent to Bi has a downshift of almost 0.5 eV, while there are negligible changes in the CBM. From Figure S12, Supporting Information, the influence of Bi on the VBM of SnSe spans a range as large as ≈200.0 Å from the nanoribbon edge.

The experimentally observed different responses of the SnSe CBM and VBM to Bi adsorption are confirmed by our DFT calculations. In Figure 3f and S13, Supporting Information, we show the calculated band structures of freestanding 2-AL SnSe upon compression and/or expansion in the AC and ZZ directions, respectively. The theoretical CBM and VBM show similar evolution trends upon lattice distortion as those observed in experiments. Based on qualitative analysis, the VBM is more easily perturbed by the in-plane lattice distortion due to the primary contribution from the in-plane p_y orbitals (Figure S14, Supporting Information). Therefore, both our experimental and theoretical results demonstrate that Bi adsorption causes lattice distortion of SnSe, which induces changes in its electronic structure; these results consistently support our deduction that Bi pulls SnSe surface atomic chains up, indicating that a strong interaction potentially occurs between the Bi atoms and SnSe underneath them. Further experimental and theoretical work is needed to explore the nature of this interaction and its relationship to the emergence of the large E_g in Bi nanoribbons on SnSe.

Our experiments demonstrate that the coverage of Bi(110) nanoislands on SnSe plays a deterministic role in the appearance of the large E_g in Bi nanostructures. When we further increased the coverage of Bi(110) layers to ≈64 ± 2% by continuously depositing Bi atoms onto SnSe, the Bi(110) went through a singular insulator–metal transition into a semimetal phase. For this analysis, considering the inhomogeneous distributions of Bi nanoribbons/islands, the coverage was estimated by repeatedly examining tens of 150 × 150 nm regions to obtain a statistical value. dI/dV spectra acquired from Bi nanoribbons/islands within the examined regions demonstrate the typical electronic characteristics of Bi at that coverage. **Figure 4**a shows some representative STS spectra acquired on Bi nanostructures at four typical coverages of ≈27 ± 2%, ≈58 ± 2%, ≈64 ± 2%, and ≈73 ± 2%. When the coverage is lower than 64 ± 2%, a pronounced E_g is presented. With higher coverage, the Bi nanoribbons resume their normal semimetal-like character, exhibiting a characteristic V-shaped dip and a linear dispersion around the Fermi level (E_F) (shown by the brown and yellow–green colored curves in Figure 4a). At the critical coverage of 64 ± 2%, the

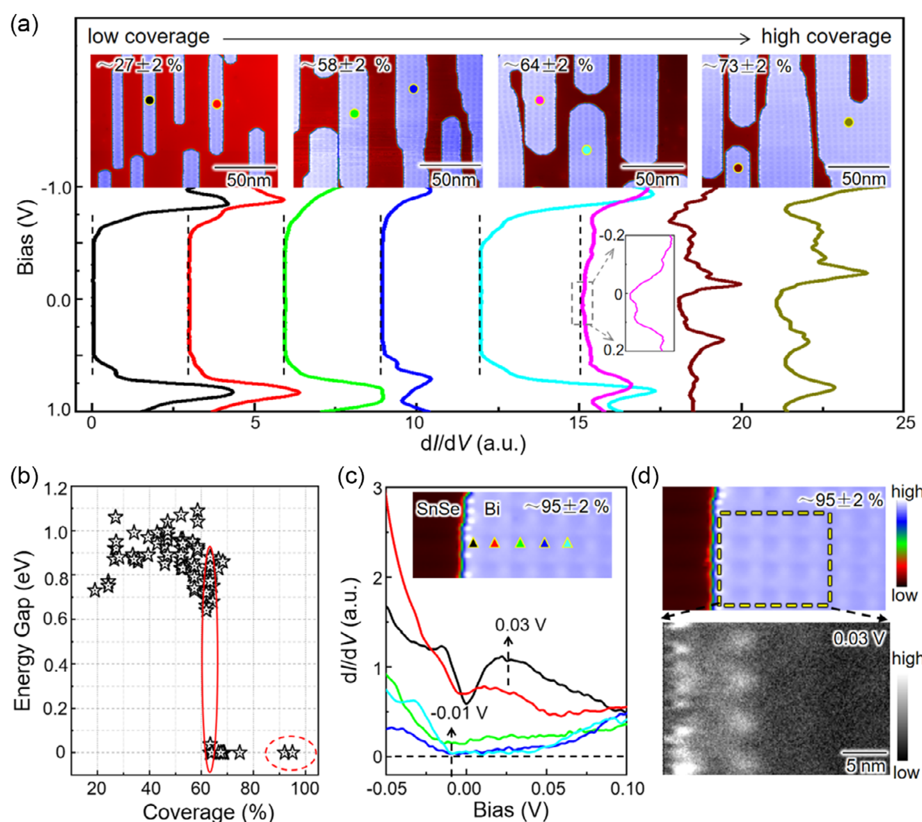

Figure 4. Energy gap of Bi(110) as a function of the coverage of Bi on SnSe. a) Series of typical STS dI/dV spectra acquired from the Bi(110) nanoribbons/islands at different coverages. Two spectra for Bi nanoislands with different sizes (highlighted in the inset images) at each coverage are shown with the corresponding colors. The two vertical black-dashed lines in the dI/dV curves at 64 ± 2% coverage mark the zero intensity of dI/dV signals. For the pink curve, the amplified dI/dV feature around E_F is shown. b) Statistical E_g values from different Bi(110) nanoribbons/islands as a function of Bi coverage. The red-lined (dashed) oval marks the data at ≈64 ± 2% (≈95 ± 2%) coverage. c) STS dI/dV spectra acquired from the edge to the interior of the Bi nanoisland in the AC direction at ≈95 ± 2% coverage. The triangles with different colors represent the measurement locations. An edge state appears at ≈0.03 V. d) STS dI/dV map at 0.03 V, showing the bright contrast at the edge of the Bi nanoisland.

© 2023 The Authors. Small Structures published by Wiley-VCH GmbH

26884062, 2023, 12, Downloaded from https://onlinelibrary.wiley.com/doi/10.1002/sstr.202300207 by RENMIN UNIVERSITY OF CHINA NON-EAL ACCOUNT, Wiley Online Library on [23/04/2024]. See the Terms and Conditions (https://onlinelibrary.wiley.com/terms-and-conditions) on Wiley Online Library for rules of use; OA articles are governed by the applicable Creative Commons License

spectra show a superposition of insulating and semimetallic Bi phases, as exhibited by the cyan and pink spectra in Figure 4a (please refer to Figure S15, Supporting Information, for more information). The cyan curve demonstrates a solid E_g similar to those acquired at coverages of ≈27 ± 2% and ≈58 ± 2%. The pink curve, however, shows a small E_g. Upon closer analysis, the pink curve clearly shows a nonzero intensity at E_F, where the V-shaped dip and linear dispersion around E_F indicate its semimetal-like characteristics. The coexistence of the two electronic phases at ≈64 ± 2% coverage is emphasized by the statistically measured E_g values from various Bi(110) nanostructures as a function of Bi coverage, as denoted by the red oval in Figure 4b. At the coverage of ≈73 ± 2%, all the Bi islands present obvious semimetal-like characteristics, regardless of their size or width, as demonstrated in the brown and yellow–green dI/dV spectra.

For the semimetal Bi(110), the theoretical and experimental results exhibit good consistency. AFM data for a nearly full coverage (≈95 ± 2%) sample show that the semimetal Bi(110) also has the DBP structure with a Bi(110)-11 × 11/SnSe(001)-12 × 12 Moiré superlattice, where the measured maximum Δh is ≈6.2 ± 1.5 pm. This DBP structure is effectively reproduced by our DFT calculations of full coverage 2-AL Bi(110) on SnSe.[40] A closer analysis of the dI/dV spectra (Figure 4c) acquired from the interior of a Bi nanoisland shows a dip at ≈−0.01 V and an asymmetric "V" shape around the dip, which is in agreement with the DFT-calculated semimetal character. When approaching the edge of the Bi nanoribbon, an evident edge state appears at 0.03 V, which sharpens the characteristic dI/dV feature into a symmetric V-shape around E_F. The edge state presents a bright contrast at the edge of the islands in the STS dI/dV mapping image (Figure 4d), consistent with the DFT-predicted atomic buckling-modulated topological electronic phase of free-standing 2-AL Bi(110).[13–16] Consequently, DFT calculations reproduce the atomic and electronic structures of the semimetal-like Bi on SnSe well. However, the emergence of the large E_g and the subsequent transition as a function of the Bi coverage require further theoretical investigation; multiple factors, such as the strong interfacial interaction between Bi and SnSe, the Moiré potentials formed in Bi/SnSe superlattices, and the possible electron–electron correlations, need to be comprehensively considered.

3. Conclusion

Our extensive experimental work has demonstrated that the above unusual phenomena generally occur for Bi(110) nanostructures grown on insulating substrates that possess DBP structures. Based on the concept of utilizing substrates with the DBP structure to create large E_g Bi(110) semiconductors, we selected SnS(001), which is a structural analog to SnSe(001),[30–35,41–45] to grow Bi(110) nanoribbons. Our results (Figure S16, Supporting Information) show that Bi(110) nanoribbons on SnS have semiconducting characteristics with an energy gap as large as ≈2.3 eV, which is even larger than the measured gap of SnS (1.1–1.5 eV).[34,35,41,42] Similarly, the large E_g in Bi(110) on SnS(001) vanishes when the coverage of Bi(110) atomic thin films is above ≈80 ± 2% (Figure S16, Supporting Information). We anticipate that these phenomena may emerge in Bi(110) on a series of group IV monochalcogenides MX (M = Sn or Ge and X = S or Se) that possess DBP structures. Future research on understanding the factors that cause the emergence of the large E_g and the insulator–metal-like transition could provide a promising avenue for designing and creating quantum materials, including but not limited to Bi on MX, with interesting electronic properties for engineering novel quantum devices.

4. Experimental Section

Sample Preparation: The high-quality SnSe and SnS single crystals used in the experiments were home grown using the temperature gradient growth method from high-purity (99.9999%) Sn, Se, and S granules. First, Sn and Se (Sn and S) granules with the stoichiometry of SnSe (SnS) and a total weight of 30 g were loaded into a quartz ampoule with an inner diameter of 11 mm. Then, the ampoule was evacuated to $<5 \times 10^{-5}$ Torr and sealed. The primary ampoule was inserted into a quartz tube, which was evacuated and sealed to protect the sample and ampoule. The double-sealed quartz tube was loaded into a tubular furnace at a 15° angle from the horizontal plane. In the furnace, the sample was slowly heated to 980 °C over 30 h, maintained at this temperature for 48 h, and then cooled from 980 to 500 °C at a precisely controlled rate of 1 °C h^{-1}. After the furnace was cooled to RT, the synthesized SnSe and/or SnS single crystals were removed from the quartz ampoule and exposed to air.

Prior to STM experiments, the SnSe (SnS) crystals were cleaved in situ in a preparation chamber under ultrahigh vacuum (UHV) conditions at RT. Bi atoms (99.999% purity, Sigma–Aldrich) were evaporated from a resistively heated evaporator onto the freshly cleaved SnSe (SnS) surface. The SnSe (SnS) substrates were kept at RT during evaporation. The prepared samples were immediately transferred into the STM chamber and cooled to 5.0 K.

STM and AFM Measurements: The STM, AFM, and spectroscopy experiments were carried out in UHV low-temperature STM system (CreaTec) at liquid He temperature. STM topographic images were acquired in the constant-current mode. The dI/dV spectra were measured using the standard lock-in technique with a bias modulation of 8 mV at 321.333 Hz. The STM tips were chemically etched with tungsten and spectroscopically calibrated against the Shockley surface states of cleaned Cu(111) or Au(111) surfaces before being utilized on Bi/SnSe or Bi/SnS. AFM imaging was performed via frequency modulation with a constant amplitude of $A = 120$ pm. The resonance frequency of the AFM probe was $f_0 = 24.5$ kHz, and its quality factor was $Q = 53\,764$ at ≈5.0 K.

DFT Calculations: DFT calculations were performed using the generalized gradient approximation with the Perdew–Burke–Ernzerhof (PBE) functional[46] for the exchange-correlation potential, the projector augmented wave method,[47] and a plane-wave basis set as implemented in the Vienna ab initio simulation package (VASP).[48] Dispersion corrections were performed at the van der Waals density functional (vdW-DF) level[49] with the optB86b functional for the exchange potential (optB86b-vdW)[50] in all structural relaxations. The structures were fully relaxed until the residual force per atom was less than 0.001 eV Å^{-1}. The PBE functional was used in the electronic structure calculations based on the optimized atomic structures using the optB86b-vdW functional. All electronic properties were calculated with consideration of spin–orbit coupling. Energy cutoffs for plane waves of 700 and 550 eV were used for structural relaxation and electronic structure calculations, respectively. For 2-AL SnSe, a sufficiently large vacuum layer of over 15 Å along the out-of-plane direction was used to eliminate the interaction among layers. The uniaxial epitaxial strain along the AC (ZZ) direction was achieved by varying the lattice constant in the AC (ZZ) direction to a given value and keeping the lattice constant in the ZZ (AC) direction unchanged.

© 2023 The Authors. Small Structures published by Wiley-VCH GmbH

26884062, 2023, 12, Downloaded from https://onlinelibrary.wiley.com/doi/10.1002/sstr.202300207 by RENMIN UNIVERSITY OF CHINA NON-EAL ACCOUNT, Wiley Online Library on [23/04/2024]. See the Terms and Conditions (https://onlinelibrary.wiley.com/terms-and-conditions) on Wiley Online Library for rules of use; OA articles are governed by the applicable Creative Commons License

Supporting Information

Supporting Information is available from the Wiley Online Library or from the author.

Acknowledgements

Q.Y. and Y.L. contributed equally to this work. Q.Y. and Y.L. grew the Bi samples and performed scanning tunneling microscopy measurements. D.P.G. and W.J. performed first-principles calculations. The authors gratefully acknowledge the productive discussions with Chunwei Lin and Rui Yu. This work was supported by the Strategic Priority Research Program of the Chinese Academy of Sciences (grant no. XD30000000), the National Key R&D Program of China (grant nos. 2018YFA0305802 and 2017YFA0303500), the National Natural Science Foundation of China (grant nos. 11774267, 61674171, 11974422), and the Fundamental Research Funds for the Central Universities and the Research Funds of Renmin University of China [grant no. 22XNKJ30 (W.J.)]. D.P.G. was supported by the Outstanding Innovative Talents Cultivation Funded Programs 2022 of Renmin University of China. Calculations were performed at the Physics Lab of High-Performance Computing of Renmin University of China.

Conflict of Interest

The authors declare no conflict of interest.

Data Availability Statement

The data that support the findings of this study are available from the corresponding author upon reasonable request.

Keywords

Bi(110), energy gaps, insulator–metal transitions, qPlus atomic force microscopy, scanning tunneling microscopy, SnSe

Received: June 13, 2023
Revised: July 30, 2023
Published online: August 29, 2023

[1] Y. Guo, Y.-F. Zhang, X.-Y. Bao, T.-Z. Han, Z. Tang, L.-X. Zhang, W.-G. Zhu, E. G. Wang, Q. Niu, Z. Q. Qiu, J.-F. Jia, Z.-X. Zhao, Q.-K. Xue, *Science* **2004**, *306*, 1915.
[2] F. Reis, G. Li, L. Dudy, M. Bauernfeind, S. Glass, W. Hanke, R. Thomale, J. Schafer, R. Claessen, *Science* **2017**, *357*, 287.
[3] J. Gou, B. Xia, H. Li, X. Wang, L. Kong, P. Cheng, H. Li, W. Zhang, T. Qian, H. Ding, Y. Xu, W. Duan, K. Wu, L. Chen, *Phys. Rev. Lett.* **2018**, *121*, 126801.
[4] K. Chang, J. Liu, H. Lin, N. Wang, K. Zhao, A. Zhang, F. Jin, Y. Zhong, X. Hu, W. Duan, Q. Zhang, L. Fu, Q. K. Xue, X. Chen, S. H. Ji, *Science* **2016**, *353*, 274.
[5] Z. Qin, J. Pan, S. Lu, Y. Shao, Y. Wang, S. Du, H.-J. Gao, G. Cao, *Adv. Mater.* **2017**, *29*, 1606046.
[6] G. Alessio Verni, B. Long, F. Gity, M. Lanius, P. Schuffelgen, G. Mussler, D. Grutzmacher, J. Greer, J. D. Holmes, *RSC Adv.* **2018**, *8*, 33368.
[7] C. R. Ast, H. Hochst, *Phys. Rev. Lett.* **2001**, *87*, 177602.
[8] K. Behnia, L. Balicas, Y. Kopelevich, *Science* **2007**, *317*, 1729.
[9] X. Gonze, J. Michenaud, J. Vigneron, *Phys. Rev. B* **1990**, *41*, 11827.
[10] Y. Liu, R. E. Allen, *Phys. Rev. B* **1995**, *52*, 1566.
[11] O. Prakash, A. Kumar, A. Thamizhavel, S. Ramakrishnan, *Science* **2017**, *355*, 52.
[12] G. E. Smith, G. A. Baraff, J. M. Rowell, *Phys. Rev.* **1964**, *135*, A1118.
[13] Y. Lu, W. Xu, M. Zeng, G. Yao, L. Shen, M. Yang, Z. Luo, F. Pan, K. Wu, T. Das, P. He, J. Jiang, J. Martin, Y. P. Feng, H. Lin, X. S. Wang, *Nano Lett.* **2015**, *15*, 80.
[14] S. Ju, M. Wu, H. Yang, N. Wang, Y. Zhang, P. Wu, P. Wang, B. Zhang, K. Mu, Y. Li, D. Guan, D. Qian, F. Lu, D. Liu, W.-H. Wang, X. Chen, Z. Sun, *Chin. Phys. Lett.* **2018**, *35*, 077102.
[15] S. S. Li, W. X. Ji, P. Li, S. J. Hu, L. Cai, C. W. Zhang, S. S. Yan, *ACS Appl. Mater. Interfaces* **2017**, *9*, 21515.
[16] J. Wang, X. Sun, H. Du, C. Ma, B. Wang, *Phys. Rev. B* **2022**, *105*, 115407.
[17] H. T. Chu, *Phys. Rev. B* **1995**, *51*, 5532.
[18] T. Hirahara, I. Matsuda, S. Yamazaki, N. Miyata, S. Hasegawa, T. Nagao, *Appl. Phys. Lett.* **2007**, *91*, 202106.
[19] C. A. Hoffman, J. R. Meyer, F. J. Bartoli, A. Di Venere, X. J. Yi, C. L. Hou, H. C. Wang, J. B. Ketterson, G. K. Wong, *Phys. Rev. B* **1993**, *48*, 11431.
[20] Y. M. Koroteev, G. Bihlmayer, J. E. Gayone, E. V. Chulkov, S. Blugel, P. M. Echenique, P. Hofmann, *Phys. Rev. Lett.* **2004**, *93*, 046403.
[21] J.-Y. Liu, H.-H. Sun, D.-D. Guan, Y.-Y. Li, S.-Y. Wang, C.-H. Liu, H. Zheng, J.-F. Jia, *Acta Phys. Sin.* **2018**, *67*, 170701.
[22] J. Gou, L. Kong, X. He, Y. L. Huang, J. Sun, S. Meng, K. Wu, L. Chen, A. T. S. Wee, *Sci. Adv.* **2020**, *6*, eaba2773.
[23] T. Hu, X. Hui, X. Zhang, X. Liu, D. Ma, R. Wei, K. Xu, F. Ma, *J. Phys. Chem. Lett.* **2018**, *9*, 5679.
[24] R. Ludeke, *J. Vac. Sci. Technol. B* **1989**, *7*, 936.
[25] Y. Xi, M. Zhao, H. Feng, Y. Sun, X. Man, X. Xu, W. Hao, S. Dou, Y. Du, *J. Phys.: Condens. Matter* **2021**, *34*, 074003.
[26] L. Peng, J. Qiao, J. J. Xian, Y. Pan, W. Ji, W. Zhang, Y. S. Fu, *ACS Nano* **2019**, *13*, 1885.
[27] T. Nagao, J. T. Sadowski, M. Saito, S. Yaginuma, Y. Fujikawa, T. Kogure, T. Ohno, Y. Hasegawa, S. Hasegawa, T. Sakurai, *Phys. Rev. Lett.* **2004**, *93*, 105501.
[28] P. J. Kowalczyk, S. A. Brown, T. Maerkl, Q. Lu, C.-K. Chiu, Y. Liu, S. A. Yang, X. Wang, I. Zasada, F. Genuzio, T. O. Menteş, A. Locatelli, T.-C. Chiang, G. Bian, *ACS Nano* **2020**, *14*, 1888.
[29] J. T. Sun, H. Huang, S. L. Wong, H. J. Gao, Y. P. Feng, A. T. Wee, *Phys. Rev. Lett.* **2012**, *109*, 246804.
[30] G. Duvjir, T. Min, T. Thi Ly, T. Kim, A.-T. Duong, S. Cho, S. H. Rhim, J. Lee, J. Kim, *Appl. Phys. Lett.* **2017**, *110*, 262106.
[31] S.-U. Kim, A.-T. Duong, S. Cho, S. H. Rhim, J. Kim, *Surf. Sci.* **2016**, *651*, 5.
[32] L. D. Zhao, S. H. Lo, Y. Zhang, H. Sun, G. Tan, C. Uher, C. Wolverton, V. P. Dravid, M. G. Kanatzidis, *Nature* **2014**, *508*, 373.
[33] L.-D. Zhao, C. Chang, G. Tan, M. G. Kanatzidis, *Energy Environ. Sci.* **2016**, *9*, 3044.
[34] A. Dewandre, M. J. Verstraete, N. Grobert, Z. Zanolli, *J. Phys.: Mater.* **2019**, *2*, 044005.
[35] L. C. Gomes, A. Carvalho, *Phys. Rev. B* **2015**, *92*, 085406.
[36] M. L. Perrin, C. J. Verzijl, C. A. Martin, A. J. Shaikh, R. Eelkema, J. H. van Esch, J. M. van Ruitenbeek, J. M. Thijssen, H. S. van der Zant, D. Dulic, *Nat. Nanotechnol.* **2013**, *8*, 282.
[37] P.-Y. Xiong, S.-Z. Chen, W.-X. Zhou, K.-Q. Chen, *Phys. Lett. A* **2017**, *381*, 2016.
[38] Y. Liu, Z. Qiu, A. Carvalho, Y. Bao, H. Xu, S. J. Tan, W. Liu, A. H. Castro Neto, K. P. Loh, J. Lu, *Nano Lett.* **2017**, *17*, 1970.
[39] D. Schreyer, H. Kim, R. Wiesendanger, *New J. Phys.* **2020**, *22*, 093013.
[40] Y. Li, Q. Yuan, D. Guo, C. Lou, X. Cui, G. Mei, H. Petek, L. Cao, W. Ji, M. Feng, *Adv. Mater.* **2023**, *35*, 2300572.

© 2023 The Authors. Small Structures published by Wiley-VCH GmbH

26884062, 2023, 12, Downloaded from https://onlinelibrary.wiley.com/doi/10.1002/sstr.202300207 by RENMIN UNIVERSITY OF CHINA NON-EAL ACCOUNT, Wiley Online Library on [23/04/2024]. See the Terms and Conditions (https://onlinelibrary.wiley.com/terms-and-conditions) on Wiley Online Library for rules of use; OA articles are governed by the applicable Creative Commons License

[41] S. Li, Y. Wang, P. Cheng, B. Feng, L. Chen, K. Wu, *Small* **2021**, *17*, e2101154.
[42] P. E. Lippens, M. El Khalifi, M. Womes, *Phys. Status Solidi B* **2017**, *254*, 1600194.
[43] T. T. Ly, G. Duvjir, T. Min, J. Byun, T. Kim, M. M. Saad, N. T. M. Hai, S. Cho, J. Lee, J. Kim, *Phys. Chem. Chem. Phys.* **2017**, *19*, 21648.
[44] Y. Li, C. Xia, J. Du, W. Xiong, X. Li, S. Wei, *Phys. Chem. Chem. Phys.* **2017**, *19*, 5423.
[45] H. Ullah, M. Noor-A-Alam, H. J. Kim, Y.-H. Shin, *J. Appl. Phys.* **2018**, *124*, 065102.
[46] J. P. Perdew, K. Burke, M. Ernzerhof, *Phys. Rev. Lett.* **1996**, *77*, 3865.
[47] P. E. Blöchl, *Phys. Rev. B* **1994**, *50*, 17953.
[48] G. Kresse, J. Furthmüller, *Phys. Rev. B* **1996**, *54*, 11169.
[49] M. Dion, H. Rydberg, E. Schröder, D. C. Langreth, B. I. Lundqvist, *Phys. Rev. Lett.* **2004**, *92*, 246401.
[50] J. Klimeš, D. R. Bowler, A. Michaelides, *Phys. Rev. B* **2011**, *83*, 195131.

© 2023 The Authors. Small Structures published by Wiley-VCH GmbH

26884062, 2023, 12, Downloaded from https://onlinelibrary.wiley.com/doi/10.1002/sstr.202300207 by RENMIN UNIVERSITY OF CHINA NON-EAL ACCOUNT, Wiley Online Library on [23/04/2024]. See the Terms and Conditions (https://onlinelibrary.wiley.com/terms-and-conditions) on Wiley Online Library for rules of use; OA articles are governed by the applicable Creative Commons License